Evaporation-residue cross sections in complete fusion reactions leading to Hg and Rn isotopes

D. Kamas,[1,2] A. Opichal,[1,3] E. V. Chernysheva,[1] S. N. Dmitriev,[1] A. V. Gulyaev,[1] A. V. Gulyaeva,[1] M. Holik,[4] J. Kliman,[2] A. B. Komarov,[1] L. Krupa,[1,4] A. S. Novoselov,[1] Yu. Ts. Oganessian,[1] A. V. Podshibyakin,[1] A. M. Rodin,[1] V. S. Salamatin,[1] S. V. Stepantsov,[1] V. Yu. Vedeneev,[1] and S. A. Yukhimchuk[1]

[1]*Flerov Laboratory of Nuclear Reactions, JINR, Dubna 141980, Russia*

[2]*Institute of Physics, SASc, Dúbravská cesta 9, 845 11 Bratislava 45, Slovakia*

[3]*Department of Experimental Physics, Faculty of Science, Palacky University, 17. listopadu 1192/12, 771 46 Olomouc, Czech Republic*

[4]*Institute of Experimental and Applied Physics, Czech Technical University, Husova 240/5, Prague 1, 110 00, Czech Republic*

(Received 15 August 2019; revised 21 December 2021; accepted 25 March 2022; published 18 April 2022)

The complete-fusion excitation functions of *xn*-evaporation channels for the reactions ^{144}Sm(^{40}Ar, *xn*)$^{184-x}$Hg, ^{148}Sm(^{36}Ar, *xn*)$^{184-x}$Hg, ^{144}Nd(^{40}Ca, *xn*)$^{184-x}$Hg, ^{142}Nd(^{48}Ca, *xn*)$^{190-x}$Hg, and ^{166}Er(^{40}Ar, *xn*)$^{206-x}$Rn have been measured by using the catcher foil technique. Its modified version as well as a corresponding software of data processing, including a deconvolution procedure to take into account effects caused by spreading the energy of the beam at its passing through absorbing foils, have been described. The measured excitation functions have been compared with ones theoretically calculated with the coupled-channel model.

DOI: 10.1103/PhysRevC.105.044612

I. INTRODUCTION

Last decades significant progress has been achieved in the nuclear physics experiments devoted to synthesis of new superheavy elements and study of their properties. The nuclides up to $Z = 118$ (Og) were synthesized in the reactions of doubly magic ^{48}Ca ions with actinide targets [1,2]. The problem of transition to synthesis of elements with $Z > 118$ is now widely discussed at new experimental facilities [3]. Among them, kinematic separators play an important role in short-lived radioactive nuclei investigations, allowing their production and identification according to their α-decay chains. Operating as velocity or energy filters, they are able to separate synthesized nuclei from background products, but without measuring, as a rule, their masses. Having this in mind, the mass separator MASHA [4] was built in FLNR, JINR, combining the ISOL [5] method for synthesis and separation of radioactive nuclei with the classical mass spectrometry technique. Though the time for identifying nuclides on this separator is slightly longer than on kinematic ones, it has made possible a direct measurement of masses of synthesized nuclides. The experiments have showed that the lifetimes of superheavy elements are quite long and amount, for example, to 3.8 s for ^{283}Cn, 29 s for ^{285}Cn, and 2.6 s for ^{289}Fl [6]. This has opened up the way for studying their chemical properties. It has been found that Cn ($Z = 112$) is more volatile than its homolog Hg [7], while Fl ($Z = 114$) differs from its light homolog Pb and exhibits the properties of the gaseous noble metal [3].

To verify experimentally the capability of the mass-separator MASHA to measure the masses of the volatile elements Cn and Fl, whose production cross sections are extremely low (about several pb), one plans to measure its efficiency for mercury as homolog of Cn, and for inert gas radon, produced as evaporation residues (ERs) in the complete fusion reactions of ^{36,40}Ar and ^{40,48}Ca heavy ions with lanthanide targets of ^{144,148}Sm, ^{142,144}Nd, and ^{166}Er.

The goal of the present work was to determine the absolute cross sections of production of these ERs, not yet available, excluding ^{148}Sm(^{36}Ar, *xn*)$^{184-x}$Hg [8], in the literature. It is known that for heavy and superheavy nuclei the fusion cross sections greatly depend on the reaction entrance channel properties such as the mass asymmetry, the charges of the interacting nuclei Z_p and Z_t, their deformations, as well as the shell closure. This dependence could be revealed itself in the production of ^{184}Hg in the reactions ^{40}Ar + ^{144}Sm, ^{36}Ar + ^{148}Sm, and ^{40}Ca + ^{144}Nd. The influence of the neutron excess in the entrance channel was investigated by comparing the production cross section of the ERs at deexcitation of the compound nucleus ^{184}Hg in the ^{40}Ca + ^{144}Nd reaction with one of the double-magic ^{48}Ca with ^{142}Nd, leading to the ^{190}Hg compound nucleus formation. The entrance channel properties of the reactions being investigated are presented in Table I.

The article is organized as follows. Section II is devoted to the experimental procedure of the cross-section measurements. In Sec. III we describe the method of processing experimental data, including the procedure for deconvolution of excitation functions. The main results and their discussion are given in Sec. IV followed by the summary in Sec. V.

II. EXPERIMENTAL DETAILS

The experiments were carried out at the U400M cyclotron of the FLNR, JINR (Dubna). Beams of ^{36}Ar, ^{40}Ar, ^{40}Ca, and ^{48}Ca with energies in the range 270–330 MeV and intensities

TABLE I. Properties of the reactions of interest: E_0: initial beam energy from the U400M cyclotron; E_{lab}: beam energy in the laboratory system at the target half layer, Z_pZ_t: product of projectile nuclear charge by target one; V_{Bass}: Bass barrier in the center-of-mass system [9]; Q_{gg}: ground-ground Q value [10]; E^*: excitation energy of the compound nucleus at the Bass barrier.

Reaction	E_0 (MeV)	E_{lab} (MeV)	Z_pZ_t	V_{Bass} (MeV)	Q_{gg} (MeV)	E^* (MeV)
$^{40}Ar + {}^{144}Sm \rightarrow {}^{184}Hg$	299	154–232	1116	129.57	−90.66	38.91
$^{36}Ar + {}^{148}Sm \rightarrow {}^{184}Hg$	324	144–233	1116	130.95	−83.22	47.73
$^{40}Ca + {}^{144}Nd \rightarrow {}^{184}Hg$	268	145–216	1200	140.11	−92.25	47.87
$^{48}Ca + {}^{142}Nd \rightarrow {}^{190}Hg$	327	202–264	1200	136.53	−98.80	37.73
$^{40}Ar + {}^{166}Er \rightarrow {}^{206}Rn$	300	156–202	1224	138.90	−90.85	48.05

of no more than 0.2 pμA were used. The beam energy was continuously measured by the time-of-flight technique using two pick-up detectors with a distance of 2 m between them, providing an energy resolution of ∼0.5%.

A step change of 3 MeV of the beam energy on the target was performed by using nickel absorber foils with the thicknesses of 2.7, 4.95, 10.3, and 16.9 μm. These foils were mounted on a mechanical feed-through construction ensuring the linear and rotational fineness of control of 0.1 mm and 0.5 °, respectively (Fig. 1). The targets were 280–330-$\mu g/cm^2$ layers of ^{144}Sm, ^{166}Er, ^{148}Sm, ^{142}Nd, and ^{144}Nd electrochemically deposited onto 680-$\mu g/cm^2$ titanium backings.

The measurement technique used in the present work is an improved version of one described in [11]. In the latter one ERs of interest produced in complete fusion reactions were implanted into a catcher foil placed downstream of the target, while bombarding ions and faster reaction products passed through it and stopped in a Faraday cup behind the foil. From time to time this foil was moved to a position in front of a detector which registered α particles coming from the decay of these reaction products.

In our experiments we replaced the above mentioned single foil catcher with an aluminum five-foil stack one, installed

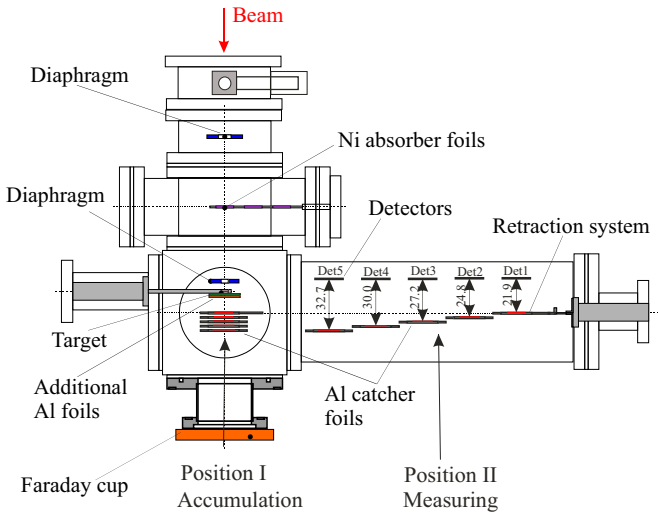

FIG. 1. Scheme of experiments. In position I the reaction products are accumulated in the catcher foils when beam is on; in position II, when beam is off, the α particles from accumulated nuclides are detected by silicon detectors.

18.2 mm behind the target. Each of these foils was circular shaped with a diameter of 20 mm and a thickness of 0.8 μm. The reaction products under investigation were implanted into the catcher and stopped at the proper foils according to their energies. To provide maximum yields of these reaction products they were made to stop close to the middle of the foil stack by placing downstream from the target two additional aluminum foils, each with a thickness of 0.8 μm. The use of five thin foils instead of a single thick one improved the α-particle energy resolution, being in the range from 70 to 100 keV [full width at half maximum (FWHM)] for five planar silicon detectors used.

The catcher stack and five silicon detectors were mounted on a specially designed retraction system. During the experiments, the catcher foils were periodically located in two positions until spectra with needed statistics were accumulated. First, for an interval of time t_B (accumulation time while the beam was on), they were packed one by one in the position I behind the target to bring to rest and gather evaporation residues of interest. Then, while the beam was off for an interval of time t_D (detection time), the foils were moved into the position II, to a face-to-face arrangement with the silicon detectors to detect the α particles from decays of these reaction products. The intervals of times t_B and t_D were chosen to be 10–30 s according to the half-lives of the ERs being studied. The transition time between two foil arrangements took no more than 0.3 s, being synchronized with both the ion beam chopping time and the data acquisition system. During the experiments the α-particle energies measured by the detectors, as well as the time signal between the start of the detection cycle and the coming time of α particles to the detectors, were recorded in a data word.

The energy signal from each silicon detector was amplified by a charge-sensitive preamplifier and then passed to a high speed 16-channel digitizer based on the PXI standard (XIA, 500 MHz, 14 bit). The information from all digitizers was read out and stored by the NI PXI controller, PXI-8119 (implemented under embedded version of Windows 7). The stored data were processed and displayed by a program running on a multimonitor PC at the control room through an internal Ethernet network. The online beam current measurement was carried out with Faraday cup and digital multimeters (NI PXIe-4081).

A control system based on CompactRIO standard was developed and used in the experiments. It synchronizes the reaction product accumulation, ion beam switching, and data

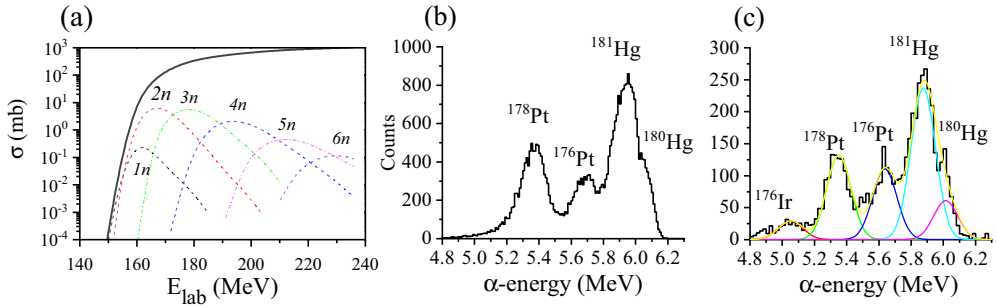

FIG. 2. (a) Excitation functions of *xn*-evaporation channels (dashed curves) and fusion cross section (thick black curve) of the reaction ^{40}Ar + ^{144}Sm calculated with the code NRV [12]; (b) energy spectrum simulated for this reaction at a projectile energy of 180 MeV and an α-particle Gaussian energy spread of 100 keV (FWHM); (c) corresponding experimental α-particle energy spectrum of the reaction with identified peaks of some isotopes when ERs stopped in the forth foil of the catcher. Single Gaussian fits are shown in colored lines.

acquisition system by sending veto signals to pneumatic linear actuators of the catcher, to the cyclotron chopper, and to the spectrometric digitizers. All parameters concerning the beam diagnostics (wave form of the beam signal, beam energy, and intensity) are written directly into the data word of the data acquisition system.

III. DATA PROCESSING

A. Monte Carlo simulation of α-particle energy spectra

The α-particle energy spectra of nuclei produced in fusion-evaporation reactions usually have a rather complicated structure due to a large number of different evaporation channels and a lot of α-radioactive daughter nuclei in the subsequent α-decay chains. The problem to resolve these spectra into separate lines being attributed to specific decaying nuclides can be rather sophisticated. To make this procedure easier a full computational experiment was performed aimed at getting Monte Carlo α spectra of the products of the reaction mentioned above. The comparison of these calculated spectra with experimental ones turned out to be very fruitful for the α-line identification.

In the case of the five-foil catcher technique used in the present experiments, a computer simulation was used as follows. Starting from the theoretical ER excitation functions of the reactions under investigation [Fig. 2(a)], resulting from the coupled-channel model [12–14], first the α-particle yields of these residues were calculated taking into account their α-decay probabilities, their half-lives, and the durations of accumulation and measurement cycles. Then the energy spectra of α particles were generated with the GEANT4 program [15] having regard to both the α particles' ionization losses at their passing through the catcher foils and the energy resolution of the silicon detectors. One of the simulated spectra for the reaction ^{40}Ar + ^{144}Sm at a beam energy of 180 MeV is presented in Fig. 2(b). The simulations proved the accessibility of the α-particle energy resolution of about 100 keV (FWHM) for nuclides' identification. For comparison, in Fig. 2(c) we show, in the case when the ERs were brought to rest in the fourth foil of the catcher stack, the corresponding experimental α-energy spectrum with indication of peaks of some isotopes. It can be seen that the pattern of the simulated spectrum is similar to the experimental one. The details of the procedure of obtaining the latter spectrum will be described in the next sections.

As a result of the simulations we obtained the expected α-particle energy spectra for several beam energies for all reactions studied, and through this the detector resolution needed for isotope identification was estimated.

B. Isotope identification and determination of absolute cross sections

The experimental α-particle energy spectra of the ^{40}Ar + ^{144}Sm reaction products are shown in Fig. 3 for detectors 1–5. The consequence of using an array of five thin foils, apart from an improvement of the energy resolution of α-particle spectra, is the possibility to measure the range

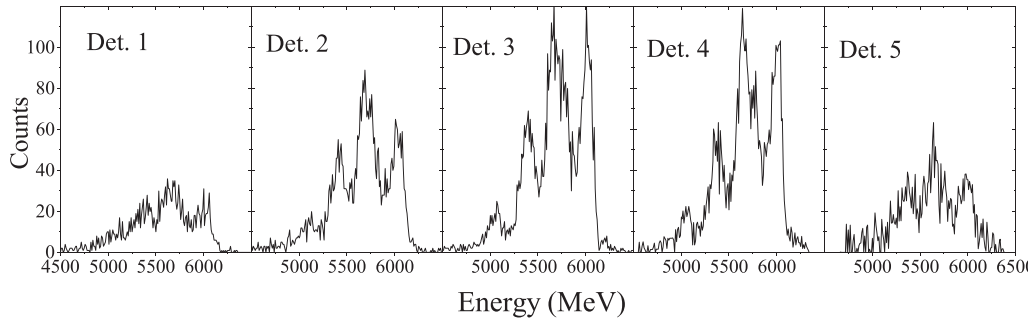

FIG. 3. Experimental α-particle spectra of the ERs for the reaction ^{40}Ar + ^{144}Sm at the projectile energy E_{lab} = 187 MeV for foils 1–5, registered by corresponding silicon detectors.

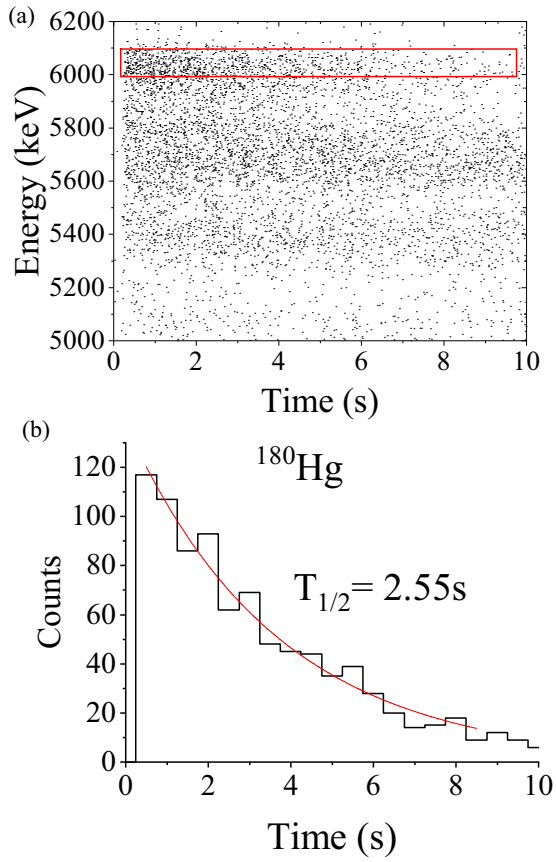

FIG. 4. (a) Two-dimensional scatter plot of the α-particle energies vs their times of registration for the reaction ^{40}Ar + ^{144}Sm at the beam energy of $E_{\rm lab} = 187$ MeV, accumulated in the third foil of the catcher array; (b) decay curve for the cut in the scatter plot.

distribution of the reaction products. Using the Gaussian function fitting procedure these spectra were then forced, in the frame of ORIGINPRO software [16], to decomposition with extracting the contributions from the ERs under study.

Since the detection times of α particles with respect to the start of each accumulation cycle were recorded in the experiment, the isotopes were identified both by α-particle energies and half-lives of α-decaying ERs. The correlated α-decay mother-daughter relationships were also analyzed to get additional information for nuclide identification. A typical two-dimensional matrix of α-particle energy vs recording time is presented in Fig. 4(a), whereas the decay curve of the mercury isotope ^{180}Hg for events in the cut is shown in Fig. 4(b).

The areas under the Gaussian curves corresponding to different α-radioactive nuclides produced in the investigated reactions were then summarized for all five detectors taking into account their geometrical efficiencies, which were simulated in GEANT4 code proposing that the α-decaying nuclides were equally distributed along the catcher foils. During the measurement time when the retraction system was in the unfolded state, the distance from each foil to its detector increased monotonically from 21.9 mm for the first detector to 32.7 mm for the fifth detector, and the detection geometrical efficiencies for silicon detectors 1–5 were 4.90, 3.95, 3.37, 2.84, and 2.43%, correspondingly.

The cross sections of the reactions, normalized to the integral from the Faraday cup, were calculated by taking into account the half-lives and α-decay probabilities of the decaying nuclides.

To determine the corrections associated with the isotope half-lives and accumulation as well as the measurement cycle times, a following procedure was applied. Denote the duration of one measurement cycle by T, which is equal to $t_B + 2t_m + t_D$, where t_B is the accumulation time, t_D is the detection time, and t_m is the time it takes the retraction system to move the catcher from the irradiation area to the detection one or equally vice versa. During one experimental run approximately one thousand cycles were carried out. In this case the loading of the aluminum foils by short lived isotopes till saturation took place very quickly.

If N_0 is the number of nuclei in any foil at saturation, then the number N of nuclei remaining in it after time t_B is

$$N = N_0 \exp(-\lambda t_B)\,. \tag{1}$$

The additional number of nuclei produced during this time is

$$N_B = \frac{\beta\sigma i}{\lambda}[1 - \exp(-\lambda t_B)], \tag{2}$$

where β – effective target thickness; σ – cross section, λ – decay constant of the studied isotope, and i – beam particle current. So, when the detection period starts, $N + N_B$ nuclei have been implanted already into the foil. In the stationary regime, N_0 can be calculated from three sequential Eqs. (3)–(5):

$$(N + N_B)\exp[-\lambda(2t_m + t_D)] = N_0, \tag{3}$$

$$[N_0 \exp(-\lambda t_B) + N_B]\exp[-\lambda(2t_m + t_D)] = N_0, \tag{4}$$

$$N_0 = \frac{N_B \exp[-\lambda(2t_m + t_D)]}{1 - \exp(-\lambda T)}. \tag{5}$$

The number N_D of nuclei in the foil when the detection period starts is then

$$\begin{aligned} N_D &= N_0 \exp[\lambda(t_m + t_D)] \\ &= \frac{\beta\sigma i}{\lambda}[1 - \exp(-\lambda t_B)]\left(\frac{\exp(-\lambda t_m)}{1 - \exp(-\lambda T)}\right). \end{aligned} \tag{6}$$

The number of α particles $N^{\alpha}_{\rm det}$ registered during one detection period is

$$\begin{aligned} N^{\alpha}_{\rm det} &= g\varepsilon_\alpha N_D[1 - \exp(-\lambda t_D)] \\ &= \frac{g\varepsilon_\alpha\beta\sigma i}{\lambda}\frac{\exp(-\lambda t_m)[1 - \exp(-\lambda t_B)][1 - \exp(-\lambda t_D)]}{1 - \exp(-\lambda T)}, \end{aligned} \tag{7}$$

where g is the geometrical efficiency of the detector and ε_α is the α-decay branching ratio. So, the cross section for the production of a nucleus can be calculated in the following

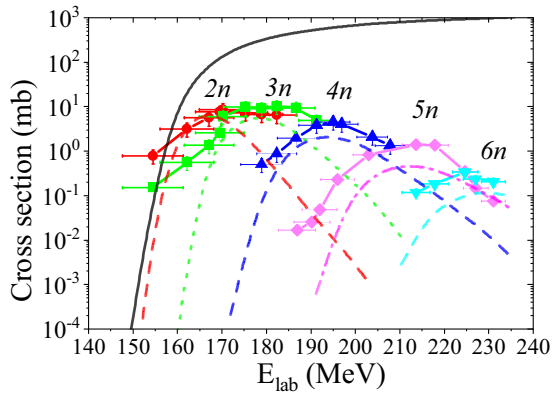

FIG. 5. Cross sections of xn-evaporation channels of the reaction ^{40}Ar + ^{144}Sm measured by using the five-foil catcher method: ($2n$: red circles; $3n$: green squares; $4n$: blue up triangles; $5n$: purple rhombuses; $6n$: cyan down triangles). Dashed curves are the cross sections calculated by the coupled-channel model [12]. Black solid line is the fusion cross section.

way:

$$\sigma = \frac{N^{\alpha}_{\rm det}\lambda[1-\exp(-\lambda T)]}{g\beta\varepsilon_{\alpha} i[1-\exp(-\lambda t_B)]\exp(-\lambda t_m)[1-\exp(-\lambda t_D)]}. \quad (8)$$

Going from the beam particle current i to the integral from Faraday cup J, the formula can be rewritten as

$$\sigma = \frac{N^{\alpha}_{\rm run}\lambda t_B[1-\exp(-\lambda T)]}{g\beta\varepsilon_{\alpha}\, J[1-\exp(-\lambda t_B)]\exp(-\lambda t_m)[1-\exp(-\lambda t_D)]}, \quad (9)$$

where $N^{\alpha}_{\rm run}$ is the number of α-decays of the selected nuclide during the experimental run.

In each case the beam energy in the middle of the target was calculated by taking into account its energy losses in the nickel absorbing foils, the Ti backing, and the half depth of the target layer. The calculations were performed for every run with SRIM software [17] using the results of online beam energy measurements. The excitation functions for the reaction ^{40}Ar + ^{144}Sm obtained with such a procedure as well as the coupled-channel model are shown in Fig. 5. The experimental cross-section errors were calculated as the square root of the quadratic sum of statistical errors, beam intensity, and target thickness uncertainties.

By looking at Fig. 5, one can see a difference in the shapes of the theoretical cross sections calculated by the coupled-channel model and the measured ones. Certainly, this difference in the excitation function shapes deals with the fact that in theoretical calculations the energy spreading of heavy ion beams in the nickel absorbing foils, which takes place in the experiments, is not considered. This effect is more significant at a higher amount of absorbed energy and hence in the low energy region, especially in the vicinity of the Coulomb barrier, where the excitation curves fall down sharply.

C. Excitation functions corrected for beam energy spread

The problem of influence of the beam energy spread on excitation functions has been discussed in [18]. This spread is caused both by the initial energy spread of the ion beam from the accelerator and by additional energy widening during the pass through absorbers, target, and backing. This effect does not affect so much the region of excitation function maximum, but can be significant to the left of it, where this function falls down very steeply.

In the present experiments the overall variation of the beam energy from the exit of the U400M cyclotron to the center of the target amounted to 100–180 MeV (Table I) using the Ni absorber foils.

We carried out an additional experiment to measure the spread of the ^{40}Ar beam at its passing through the matters of different thicknesses. In this experiment a ^{144}Sm target of 320 μg/cm^2, deposited on a 680 − μg/cm^2 Ti backing, as well as an absorbing 10.3 μm-thick Ni foil were used. The final beam energy was measured by a silicon detector. Three measurements were performed, one without the foil and the target, and two with the Ni foil and the target. In the first case the measured beam energy spread turned out to be 4.7 MeV (FWHM). After installing the Ni foil and the target the energy spread increased to 11.7 MeV (FWHM). Then, by rotating the Ni foil through 45 ° this spread almost doubled to a value of 21.5 MeV (FWHM), which is more than its initial value by a factor of 4.

To eliminate the influence of the beam energy spread on the excitation functions the Gold deconvolution method [19] was applied taking into account the beam energy broadening obtained in this additional experiment. A software was developed using the TSpectrum class of ROOT [20]. The Gaussian response of the beam energy spreading as a function of the energy E was used:

$$D(E) = \frac{1}{\sigma\sqrt{2\pi}} e^{-(1/2)[(E-E_c)/\sigma]^2}, \quad (10)$$

where E_c is the average beam energy in the middle of the target and σ is one standard deviation, which was chosen as

$$\sigma(E) = Ae^{-kE} + \sigma_0, \quad (11)$$

and parameters A, k, and σ_0 were obtained by fitting the experimental data of the experiment with the ^{40}Ar beam. Then the matrix elements of our response function can be written as

$$h^{ij} = C^j e^{-2[(E^i - E_c{}^j)/\sigma]^2}, \quad (12)$$

where C^j are the normalization constants,

$$C^j = \frac{1}{\sum_i e^{-2[(E^i - E_c{}^j)/\sigma]^2}}, \quad (13)$$

and E^i and $E_C{}^j$ are i-row and j-column energies in the matrix. During the deconvolution procedure each row of the matrix h^{ij} was normalized to unity to preserve the integral value under the cross-section curves.

The excitation functions after applying the deconvolution procedure are shown in Fig. 6 for the reaction ^{40}Ar + ^{144}Sm. One can see a considerable decrease of experimental cross-section values in the close vicinity of the Coulomb barrier.

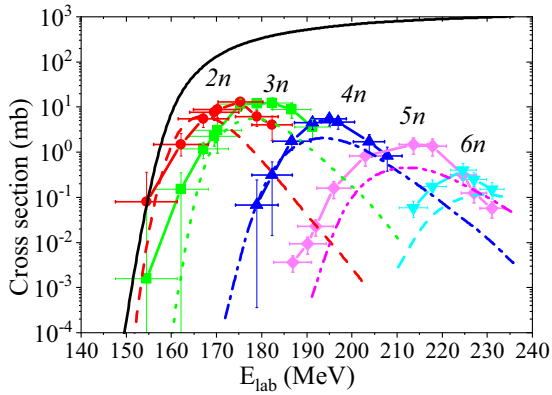

FIG. 6. The same as in Fig. 5, but after corrections on the beam energy spread using the deconvolution method.

The excitation function curves are now more similar to the calculated ones (dashed curves). This proves a usefulness of the deconvolution method for the experiments with high spreads of the beam energy. The errors caused by applying this procedure were included in ones in Fig. 6. Furthermore, the deconvolution procedure was applied for all reactions studied. The Gaussian functions of energy spreads for other beams (^{36}Ar, ^{40}Ca, and ^{48}Ca) were obtained using Eq. (11) and then normalized to ratios of the theoretical energy spread values to the experimental ones measured for the ^{40}Ar beam.

IV. RESULTS AND DISCUSSION

Measured excitation energy functions for the reactions ^{40}Ar + ^{144}Sm, ^{36}Ar + ^{148}Sm, ^{40}Ca + ^{144}Nd, ^{48}Ca + ^{142}Nd, and ^{40}Ar + ^{166}Er, corrected for the beam energy spread, are shown in Figs. 7–9. The cross-section points are drawn by colored symbols and linked by lines, whereas the theoretical ER cross-section curves calculated with the coupled-channel model and the statistical model of decay of excited nuclei [12–14] are shown with dashed lines. The fusion cross sections are drawn by solid lines. The experimental errors for the excitation functions are like in Fig. 6, and they are not presented in Figs. 7–9 for better clarity.

The 2*n* and 3*n* channels, having the maximum values of the cross sections close to each other, dominate in the reaction ^{40}Ar + ^{144}Sm [Fig. 7(a)]. The cross sections of the channels with a higher number of evaporated neutrons gradually decrease because of an enhanced probability of fission from higher energy excited states.

A similar behavior can be seen in the reaction ^{36}Ar + ^{148}Sm [Fig. 7(b)] which leads to the same compound nucleus ^{184}Hg. However, unlike the reaction ^{40}Ar + ^{144}Sm, which is between two spherical nuclei [with a ^{184}Hg excitation energy of 39 MeV at the Bass barrier (V_B) of the reaction], here both nuclei are deformed (see Table II). In this case the Coulomb barrier depends on the mutual orientation of interacting nuclei, and the compound nucleus excitation energy at the Coulomb barrier ranges from 42 MeV for the polar orientation (V_P) to 49 MeV for the equatorial one (V_{Eq}). Deformation parameters of all nuclei involved are listed in Table II. Because both interacting nuclei in reactions ^{36}Ar + ^{148}Sm are only slightly deformed, the theoretical calculations with NRV code [12–14] were performed with excitation of two quadrupole and one octupole phonons for both nuclei. In the case of the ^{40}Ar + ^{144}Sm reaction two quadrupole and one octupole phonons in ^{40}Ar and one quadrupole and one octupole phonons in ^{144}Sm nuclei were proposed to be excited.

The ^{40}Ca + ^{144}Nd reaction [Fig. 8(a)] leads also to the same $^{184-x}$Hg isotopes as in the case of ^{40}Ar + ^{144}Sm and ^{36}Ar + ^{148}Sm. It is a reaction between two spherical nuclei, as in the former of the just mentioned ones, but with a different ratio of protons to neutrons in the projectile and target nuclei. Its target nucleus does not have a closed neutron shell comparing to ^{40}Ar + ^{144}Sm, i.e., it is not the magic nucleus. Since the magic nuclei exhibit an enhanced stability, it is therefore necessary to check how this effect is reflected in the measured

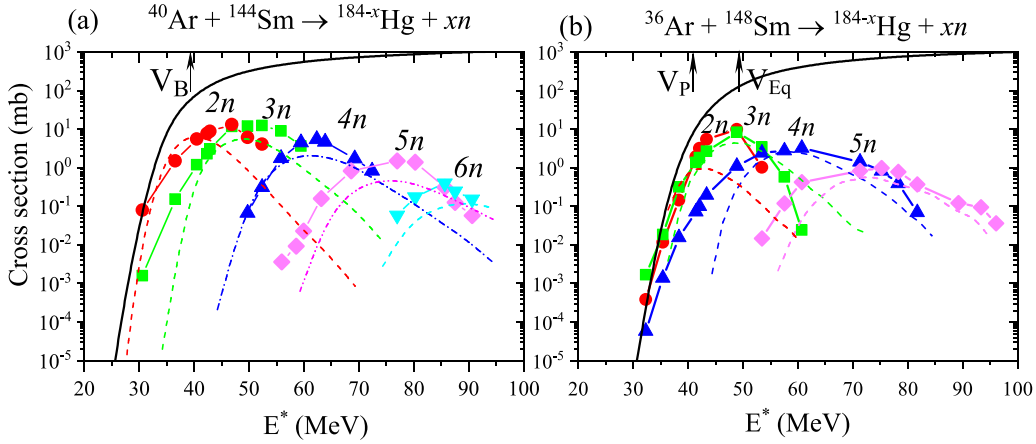

FIG. 7. Cross sections (symbols) of *xn*-evaporation channels (2*n*: red circles; 3*n*: green squares; 4*n*: blue up triangles; 5*n*: purple rhombuses; 6*n*: cyan down triangles) of the reactions: (a) ^{40}Ar + ^{144}Sm and (b) ^{36}Ar + ^{148}Sm, measured by the five-foil catcher method versus compound nucleus excitation energy. The theoretical excitation functions are drawn by dashed lines. V_B is the Bass barriers for spherical interacting nuclei, V_P and V_{Eq} are the Coulomb barriers for polar and equatorial mutual orientation of deformed ones, respectively. Fusion cross sections are shown by solid lines.

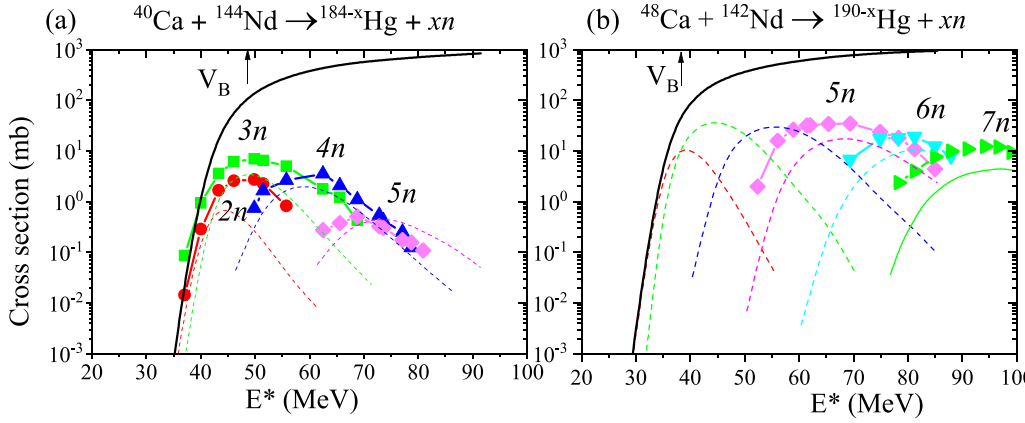

FIG. 8. The designations are the same as in Fig. 7 but for (a) ^{40}Ca + ^{144}Nd and (b) ^{48}Ca + ^{142}Nd reactions.

excitation functions. At the transition from the reaction between Ar + Sm to the reaction of Ca + Nd, the factor Z_pZ_t increases from 1116 to 1200. So, first, what we can notice when comparing Figs. 7(a) and 8(a) is a shift in the positions of the Coulomb barrier of the reactions from 39 to 48 MeV. This affects mostly the 2n-channel position and its maximum cross-section value which is lower than in the case of the 3n channel. However, the experimentally determined 2n-channel cross section is slightly higher than the theory predicts, similar to the ^{36}Ar + ^{148}Sm reaction. In the theoretical calculations one quadrupole and one octupole phonon in ^{40}Ca as well as two quadrupole phonons and one octupole phonon in ^{144}Nd were taken as excited.

In the reaction ^{48}Ca + ^{142}Nd, with a ^{190}Hg compound nucleus excitation energy of 38 MeV at the Coulomb barrier [Fig. 8(b)], only the high mass $^{183\text{-}185}$Hg isotopes were observed. The channels with lower numbers of evaporated neutrons were not registered because they led to Hg isotopes, which do not undergo α decay. The excitation of one quadrupole phonon in ^{48}Ca and two quadrupole phonons and one octupole phonon in ^{142}Nd were suggested to be excited in the calculation of the theoretical cross sections.

In Fig. 9 the excitation energy functions of the ^{40}Ar + ^{166}Er reaction are shown for some xn- and pxn-evaporation channels. These ER cross sections are less by a factor of about 10 as compared to the reactions on samarium and neodymium lanthanide targets. It seems to be an indication of a greater fissility of the radon compound nucleus ^{206}Rn than the mercury ones ^{184,190}Hg. Two quadrupole and one octupole phonons in ^{40}Ar and the static deformation of ^{166}Er were accounted for in the theoretical calculations [12–14]. The thick black lines represent the calculated total complete-fusion cross sections. Since both the cross-section and beam energy errors for all reactions studied were similar to that shown in Fig. 6, they are not shown in Fig. 9.

In the reaction ^{40}Ar + ^{166}Er [Fig. 9(a)], for which the ^{206}Rn compound nucleus excitation energy is 39 MeV at the Coulomb barrier for the polar orientation of the interacting nuclei (V_P) and 52 MeV for the equatorial one (V_{Eq}), the 3n channel reaches its highest value. The cross sections of channels with a higher number of evaporated neutrons gradually decreases, as in the previous reactions, whereas the measured 1pxn evaporation channel cross sections have values of the same order of magnitude, with the maximum for the 1p3n channel [Fig. 9(b)]. The maximum values of the excitation functions and their positions for all reactions are listed in Table III.

Figure 10 shows the maxima of the excitation functions of the reactions studied in dependence on the isotope mass A. The red lines show calculations with the coupled-channel

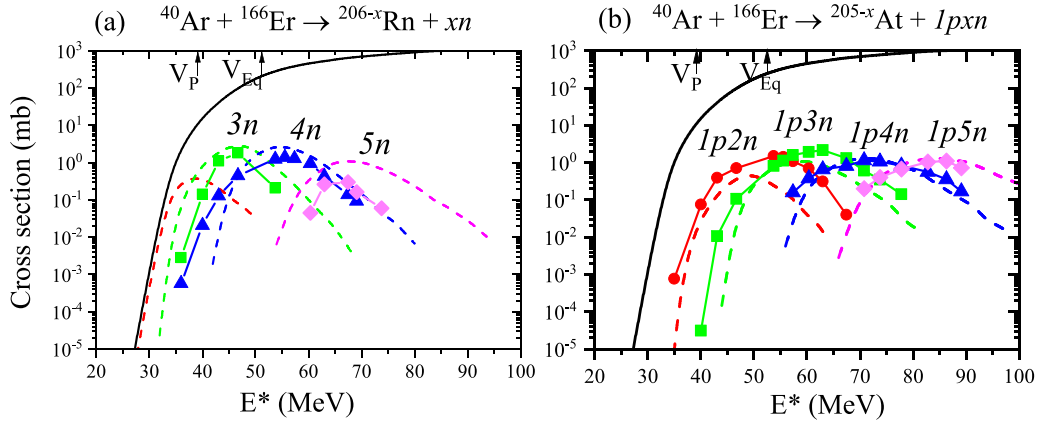

FIG. 9. Cross sections of xn- (a) and pxn- (b) evaporation channels for the reaction ^{40}Ar + ^{166}Er. The designations are the same as in Fig. 8.

TABLE II. Quadrupole deformation parameters of the nuclei under consideration [21].

Nucleus	β_2
^{36}Ar	−0.148
^{40}Ar	−0.013
^{40}Ca	0
^{48}Ca	0
^{144}Sm	0
^{148}Sm	0.175
^{142}Nd	0
^{144}Nd	0
^{166}Er	0.342

code and the statistical model of decay of excited nuclei [13,14]; the black circles show the experimental data. It can be seen that in the reactions of ^{36,40}Ar and ^{40,48}Ca projectiles on the ^{144,148}Sm and ^{142,144}Nd targets the theoretical calculations give lower values than the experimental ones, whereas for the *xn* channel of the reaction ^{40}Ar + ^{166}Er the theoretical calculations overestimate the results of the experiments.

V. SUMMARY

Evaporation-residue cross sections for the reactions ^{144}Sm(^{40}Ar, *xn*)$^{184-x}$Hg, ^{148}Sm(^{36}Ar, *xn*)$^{184-x}$Hg, ^{144}Nd(^{40}Ca, *xn*)$^{184-x}$Hg, ^{166}Er(^{40}Ar, *xn*)$^{206-x}$Rn, and ^{142}Nd(^{48}Ca, *xn*)$^{190-x}$Hg have been measured by using an improved version of the catcher foil method. ER cross sections for the reaction ^{148}Sm(^{36}Ar, *xn*)$^{184-x}$Hg were already measured in [8]. The cross sections of other reactions were measured for the first time in the present

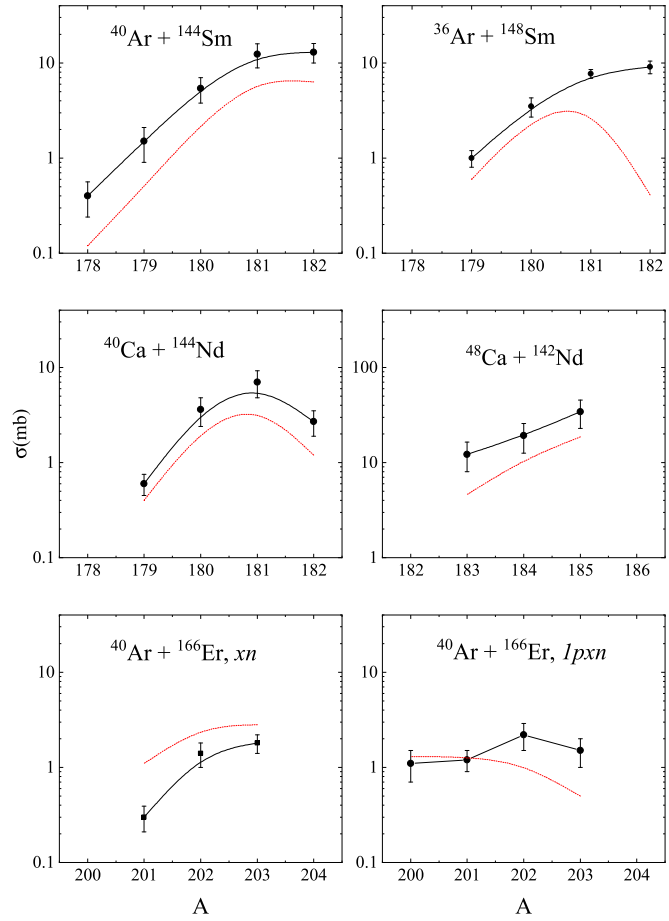

FIG. 10. The comparison of experimental (black) and theoretical (dash red lines) maxima of excitation functions for *xn* channels of the reactions ^{40}Ar + ^{144}Sm, ^{36}Ar + ^{148}Sm, ^{40}Ca + ^{144}Nd, ^{48}Ca + ^{142}Nd, and for *xn* and 1*pxn* channels in case of ^{40}Ar + ^{166}Er.

TABLE III. Cross-section maximum values in separate channels of complete fusion reactions and their positions in the excitation energy scale.

	σ(mb) (E*(MeV))					
Reaction	2*n*	3*n*	4*n*	5*n*	6*n*	7*n*
^{40}Ar + ^{144}Sm → ^{184}Hg	13.0 ± 3.0 (42.5 ± 3.3)	12.4 ± 3.5 (52.0 ± 2.6)	5.4 ± 1.6 (62.0 ± 2.3)	1.5 ± 0.6 (76.5 ± 2.2)	0.4 ± 0.2 (85 ± 2.1)	
^{36}Ar + ^{148}Sm → ^{184}Hg	9.8 ± 1.4 (46.0 ± 4.9)	8.3 ± 0.8 (48.9 ± 4.8)	3.2 ± 0.8 (60.7 ± 3.2)	1.0 ± 0.2 (75.2 ± 2.3)		
^{40}Ca + ^{144}Nd → ^{184}Hg	2.7 ± 0.8 (47.9 ± 5.7)	7.1 ± 2.2 (49.5 ± 5.7)	3.6 ± 1.2 (62.5 ± 4.1)	0.5 ± 0.2 (68.8 ± 3.8)		
^{48}Ca + ^{142}Nd → ^{190}Hg				34.4 ± 11.3 (69.4 ± 2.6)	19.2 ± 6.6 (81.2 ± 2.1)	12.2 ± 4.2 (94.1 ± 2.0)
^{40}Ar + ^{166}Er → ^{206}Rn		1.8 ± 0.4 (46.7 ± 3)	1.4 ± 0.4 (55.6 ± 2.4)	0.3 ± 0.1 (67.4 ± 2)		
^{40}Ar + ^{166}Er → ^{206}Rn	1*p*2*n* 1.5 ± 0.5 (53.7 ± 2.1)	1*p*3*n* 2.2 ± 0.7 (63.0 ± 2.1)	1*p*4*n* 1.2 ± 0.3 (70.8 ± 2)	1*p*5*n* 1.1 ± 0.4 (86.3 ± 1.9)		

work. By comparison of the ^{40}Ar + ^{144}Sm, ^{36}Ar + ^{148}Sm, and ^{40}Ca + ^{144}Nd reactions leading to the same compound nucleus ^{184}Hg, the effect of the Coulomb barrier on the position of the 2*n* channel maximum cross-section value was investigated. Slightly higher values of the experimentally determined cross sections in comparison with the coupled-channel calculated ones were shown for all reactions leading to mercury isotopes, as opposed to the reaction ^{40}Ar + ^{166}Er leading to radon isotopes, though the effect is small. The latter could be caused by rather high values of 1*pxn*-evaporation channel cross sections. One can conclude that the fission channel cross sections and other evaporation ones, like *pxn* or αxn, are lower, compared to the values predicted by the coupled-channel model, for the reactions leading to the mercury isotopes and, on the other hand, higher for the reaction ^{40}Ar + ^{166}Er leading to the radon ones.

ACKNOWLEDGMENTS

The authors thank the FLNR U400M cyclotron staff for providing the heavy ion beams necessary in the experiment and also the FLNR engineering services for ensuring the conditions essential for carrying out the given work. We are thankful to Dr. A. V. Karpov for fruitful discussions of the theoretical calculations presented by this work. The authors acknowledge the internal Grant of Palacký University (Grant No. IGA_PrF_2020_011) and the VEGA Grant Agency under Project No. 2/0181/21.

[1] Yu. Ts. Oganessian, V. K. Utyonkov, Yu. V. Lobanov, F. Sh. Abdullin, A. N. Polyakov, I. V. Shirokovsky, Yu. S. Tsyganov, G. G. Gulbekian, S. L. Bogomolov, B. N. Gikal *et al.*, Phys. Rev. C **70**, 064609 (2004).

[2] Yu. Ts. Oganessian, V. K. Utyonkov, Yu. V. Lobanov, F. Sh. Abdullin, A. N. Polyakov, R. N. Sagaidak, I. V. Shirokovsky, Yu. S. Tsyganov, A. A. Voinov, G. G. Gulbekian *et al.*, Phys. Rev. C **74**, 044602 (2006).

[3] Yu. Oganessian, Nucl. Phys. News **29**, 5 (2019).

[4] A. M. Rodin, A. V. Belozerov, D. V. Vanin , V. Yu. Vedeneyev, A. V. Gulyaev, A. V. Gulyaeva, S. N. Dmitriev, M. G. Itkis, J. Kliman, N. A. Kondratiev *et al.*, Instrum. Exp. Tech. **57**, 386 (2014).

[5] O. Kofoed-Hansen and K. O. Nielsen, Phys. Rev. **82**, 96 (1951).

[6] Yu. Ts. Oganessian, J. Phys G **34**, R165 (2007).

[7] R. Eichler, N. V. Aksenov, A. V. Belozerov, G. A. Bozhikov, V. I. Chepigin, S. N. Dmitriev, R. Dressler, H. W. Gäggeler, V. A. Gorshkov, F. Haenssler *et al.*, Nature (London) **447**, 72 (2007); R. Eichler, N. V. Aksenov, A. V. Belozerov, G. A. Bozhikov, V. I. Chepigin, R. Dressler, S. N. Dmitriev, H. W. Gäggeler, V. A.Gorshkov, F. Haenssler *et al.*, Nucl. Phys. A **787**, 373c (2007).

[8] M. Schädel, W. Brüchle, E. Jäger, A. Popeko, S. Reitmeier, E. Schimpf, R. Sagaidak, A. Shutov, A. Türler, A. Yakushev, and A. Yeremin, in *GSI Scientific Report 2003*, edited by U. Grundinger (GSI, Darmstadt, 2004), p. 20.

[9] R. Bass, Phys. Rev. Lett. **39**, 265 (1977); Lect. Notes Phys. **117**, 281 (1980).

[10] P. Möller, A. J. Sierk, T. Ichikawa, and H. Sagawa, At. Data Nucl. Data Tables **109-110**, 1 (2016).

[11] D. Vermeulen, H.-G. Clerc, C.-C. Sahm, K.-H. Schmidt, J. G. Keller, G. Münzenberg, and W. Reisdorf, Z. Phys. A **318**, 157 (1984).

[12] http://nrv.jinr.ru/nrv/.

[13] A. V. Karpov, A. S. Denikin, M. A. Naumenko, A. P. Alekseev, V. A. Rachkov, V. V. Samarin, V. V. Saiko, and V. I. Zagrebaev, Nucl. Instr. Meth. Phys. Res. A **859**, 112 (2017).

[14] V. I. Zagrebaev and V. V. Samarin, Phys. Atom. Nucl. **67**, 1462 (2004).

[15] https://geant4.web.cern.ch/.

[16] https://www.originlab.com.

[17] J. F. Ziegler, M. D. Ziegler, and J. P. Biersack, Nucl. Instr. Meth. Phys. Res. B **268**, 1818 (2010).

[18] R. N. Sagaidak and A. N. Andreyev, Int. J. Mod. Phys. E **23**, 1450001, (2014).

[19] M. Morháč, J. Kliman, V. Matoušek, M. Veselský, and I. Turzo, Nucl. Instr. Meth. Phys. Res. A **401**, 385 (1997).

[20] I. Antcheva, M. Ballintijn, B. Bellenot, M. Biskup, R. Brun, N. Buncic, Ph. Canal, D. Casadei, O. Couet, V. Fine *et al.*, Comput. Phys. Commun. **180**, 2499 (2009).

[21] http://cdfe.sinp.msu.ru/cgi-bin/muh/radcard.cgi.